BUILD SIMUL (2015) 8: 297 – 306
DOI 10.1007/s12273-015-0213-z

Simulation of indoor airflow with RAST and SST–SAS models: A comparative study

Javad Taghinia (✉), Mizanur Rahman, Timo Siikonen

School of Engineering, Aalto University, FI–00076, Epoo, Finland

Research Article

Abstract

Computational fluid dynamics (CFD) provides a suitable means to predict the air distribution characteristics in indoor spaces. This paper evaluates the performance of two turbulence models in predicting an indoor airflow: the RAST (Rahman–Agarwal–Siikonen–Taghinia) sub-grid scale model (SGS) and SST–SAS (Shear Stress Transport with Scale-Adaptive Simulation) k–ω model of hybrid RANS–LES type. These two models are applied to investigate the airflows for three ventilation scenarios: (a) forced convection, (b) mixed (natural+forced) convection and (c) isothermal impinging jet in a room. The predictions are compared with the available experimental data in the literature. However, both models produce good results but comparisons show that RAST model predictions are in better agreement with experiments due to its sensitivity toward both the resolved strain rate and vorticity parameters.

Keywords

indoor airflow,
CFD,
impinging jet,
RAST,
sub-grid scale model,
hybrid RANS–LES

Article History

Received: 23 October 2014
Revised: 30 December 2014
Accepted: 6 January 2015

1 Introduction

People spend 80%–90% of their time in an indoor environment; therefore, indoor air quality (IAQ) is an important factor affecting occupants' health and productivity. The understanding of air distribution pattern plays a key role in the design of an efficient ventilation system in enclosed spaces. Airflow in enclosed spaces is complicated due to its complex flow structures such as flow transition and turbulence. Due to these facts, a proper analysis of the velocity, temperature and turbulent characteristics of the airflow provides an essential tool to design a comfortable and efficient indoor environment in terms of thermal comfort. There are a few methods to drive the air inside an enclosed space such as forced and mixed convection flows which can be achieved via an external air supply system, producing a complex flow structure.

In recent decades, the computational fluid dynamics (CFD) method has attracted increasing attention due to its feasibility and cost effectiveness. The CFD simulation provides detailed information about significant parameters such as the velocity fluctuations, thermal distribution and jet spread rate in an indoor environment. One of the most popular CFD approaches in an indoor airflow simulation is the Reynolds Averaged Navier–Stokes (RANS) modeling. This method has gained a popularity due to its robustness and economic computing resources. The RANS requires a coarse grid as well as less computational time compared with other existing approaches (Cheng et al. 2003). However, it has a few shortcomings particularly in indoor airflow simulations with the recirculation and presence of walls. One of these drawbacks is that the RANS uses an averaging procedure, making it incapable of providing instantaneous information on turbulent structures which are essential for the thermal comfort optimization. Another limitation is the different versions of RANS turbulence models such as the one-equation model, two-equation model and second-moment models which may give good results for one case

E-mail: javad.taghiniaseyedjalali@aalto.fi

Indoor/Outdoor Airflow and Air Quality

List of symbols

C_μ	eddy-viscosity coefficient
$\overline{C}_s$	Smagorinsky coefficient
G	filter function
g	gravitational acceleration
k	total turbulent kinetic energy
Pr	molecular Prandtl number
Pr_{sgs}	sub-grid scale Prandtl number
Re	Reynolds number
$\overline{S}_{ij}$	resolved strain rate tensor
T	temperature
$\overline{u}_i$	grid filter velocity
$\overline{u}_\tau$	friction velocity
$\overline{W}_{ij}$	resolved vorticity tensor
y^+	dimensionless wall distance ($\overline{u}_\tau y / \nu$)
β	thermal expansion coefficient
$\delta_{i,j}$	Kronecker's delta
Δt	time step
$\overline{\Delta}$	grid filter width
ν, ν_T	laminar and turbulent viscosities
$\overline{\theta}_i$	grid filter temperature
ρ	density
$\tau_{i,j}$	sub-grid scale stress tensor
CFD	computational fluid dynamics
DSM	dynamic Smagorinsky model
LES	large eddy simulation
RANS	Reynolds averaged Navier–Stokes
RAST	Rahman–Agarwal–Siikonen–Taghinia
SGS	sub-grid scale

Subscripts

i, j	variable numbers
in	inlet condition
out	outlet condition

but perform poorly in another one (Chen et al. 2012). Therefore, the accuracy of results is under question, making it a difficult task for the designer to choose an appropriate and reliable approach. The performance of the various RANS turbulence models has been studied by many authors (Chen 1995, 1996, 1997; Luo and Roux 2004; Stamou and Katsiris 2006; Zhai et al. 2007; Zhang et al. 2007; Cao et al. 2011) in the literature. For example, Chen et al. (2012) investigated the airflow produced by an impinging jet in a room using different RANS models. They found that RNG k–ε model is better in predicting the flow behavior in terms of main parameters such as the velocity and temperature. Stamou and Katsiris (2006) studied the performance of SST–k–ω, RNG k–ε and standard k–ε in predicting the airflow in an office room. They concluded that the SST–k–ω model could reproduce the flow feature more accurately than that of other RANS turbulence models. In a more recent effort, Heschl et al. (2013) studied the accuracy of RANS with linear and non-linear turbulence models for different mixed ventilation settings such as the IEA Annex-20 2D room and a 3D room with a partition. They reported that the non-linear invariant of k–ε and k–ω models can capture secondary turbulence driven flow features in a more accurate manner.

Large eddy simulation (LES) can be an alternative approach to modeling and simulating of an airflow in the building. However, LES requires higher resolution and computational time compared with the RANS. Since the LES computes the time dependent flow, it can provide detailed information about turbulence properties and velocity fluctuations. The airflow in a room has a turbulent nature with separation and recirculation regions having a vital effect on the indoor air quality. The LES can reproduce these structures in a more accurate sense by including a novel and simple procedure to capture most of the turbulent structures. Considering these facts, LES can be a more suitable approach to the indoor airflow simulation than the RANS.

LES decomposes the flow field into two categories of eddy structures, namely the large scale and sub-grid scale (SGS). Large eddies are solved directly while the small ones are modeled. The SGS eddies are nearly isotropic and they are independent of the flow geometry and have a universal character. Therefore, the SGS models require fewer empirical coefficients than those of RANS models.

Different SGS models have been introduced since last three decades among which the Smagorinsky (1963) and dynamic Smagorinsky (Germano et al. 1991) models are the most popular ones. The Smagorinsky (1963) model utilizes a constant eddy-viscosity coefficient which is simple and robust, but not suitable for complex flows in which the coefficient changes with time and space. The dynamic Smagorinsky model calculates the eddy-viscosity locally varying in time and space. But this approach is not easy to implement and the encountered two-filtering procedure prevents it to be as robust as the Smagorinsky model.

The SST–SAS (Scale-Adaptive Simulation) turbulence model is a hybrid LES–RANS model developed by Menter

and Egorov (2010) which applies RANS SST k–ω close to the wall region and LES in the rest of the domain. Most of the works available in the literature are dealing with the application of RANS or other algebraic models in predicting the indoor airflow. However, to the authors' knowledge, there is almost no reported literature about the performance and application of the SST–SAS model in an indoor environment. Due to the above mentioned reason, it is beneficial and necessary to provide a benchmark solution to the performance of this method in investigating the airflow structures in an enclosed space. This paper aims at providing a computational framework on the performance of RAST (Rahman–Agarwal–Siikonen–Taghinia) SGS model (Taghinia et al. 2014a) and SST–SAS hybrid RANS–LES in an indoor airflow analysis. The RAST model with a variable eddy-viscosity coefficient is recently developed by Taghinia et al. (2014a); this model responses to the anisotropic characteristics of turbulence and non-equilibrium flows allowing the model parameter to adjust itself with a rapid change in the flow behavior, particularly close to the solid boundaries. The RAST SGS model does not require any ad hoc damping function or clipping. The objective of this current study is to evaluate the capabilities of both the RAST and SST–SAS hybrid RANS–LES models in simulating the dynamics of an indoor airflow. Three indoor airflow cases are investigated: the first and second cases deal with forced and mixed convection, respectively, in a room; the third case concentrates on the flow field in a room subjected to an airflow injected from a duct impinging on the floor. These three scenarios provide a good benchmark solution to the performance of turbulence models with various boundary conditions that are common to the room air ventilation.

2 Governing equations

2.1 Large eddy simulation (LES)

The LES model has been developed by Smagorinsky (1963). In an LES, the large eddies that carry the main fraction of energy are computed while the small eddies are modeled. This process is performed by applying a filter function $G(x;x')$ to a decomposed function f:

$$f=\overline{f}+f_{\mathrm{sgs}},\quad \overline{f}=\int_{R^3} G(x;x')f(x')\mathrm{d}x' \tag{1}$$

where the function f is decomposed to resolved (averaged) and sub-grid scale values. The filter function $G(x;x')$ herein, operated on a filter width $\overline{\Delta}$ is a top hat filter given by

$$G_i(x_i;x'_i)=\begin{cases}\dfrac{1}{\overline{\Delta}^3}, & \text{if } |x_i-x'_i|\leqslant\dfrac{\overline{\Delta}}{2},\\ 0, & \text{otherwise.}\end{cases} \tag{2}$$

Applying the spatial filter to incompressible Navier–Stokes equations and using the commutation characteristics, the LES equations yield

$$\frac{\partial\overline{u}_j}{\partial x_i}=0 \tag{3}$$

$$\frac{\partial\overline{u}_i}{\partial t}+\frac{\partial\overline{u}_i\overline{u}_j}{\partial x_j}=-\frac{1}{\rho}\frac{\partial\overline{p}}{\partial x_i}+\frac{\partial}{\partial x_j}\left(\nu\frac{\partial\overline{u}_i}{\partial x_j}\right)-\frac{\partial\tau_{ij}}{\partial x_j}+g_j\beta(\overline{\theta}-\theta_\infty)\delta_{ij} \tag{4}$$

where the subscript (∞) denotes a reference condition, g_j signifies gravitational acceleration and β is the volumetric thermal expansion coefficient (obtained from appropriate property tables). The sub-grid scale (SGS) stress tensor is defined as

$$\tau_{ij}=\overline{u_iu_j}-\overline{u}_i\overline{u}_j \tag{5}$$

The filtered energy equation is

$$\frac{\partial\overline{\theta}}{\partial t}+\frac{\partial\overline{u}_j\overline{\theta}}{\partial x_j}=\frac{\partial}{\partial x_j}\left(\frac{\nu}{Pr}\frac{\partial\overline{\theta}}{\partial x_j}\right)-\frac{\partial h_j}{\partial x_j} \tag{6}$$

where the sub-grid heat fluxes are given by

$$h_j=\overline{u_j\theta}-\overline{u}_j\overline{\theta} \tag{7}$$

The sub-grid Reynolds stresses and heat fluxes are unknown and need to be modeled.

2.1.1 *RAST sub-grid scale model*

The RAST model with a single grid filter is recently implemented for the large eddy simulation (Taghinia et al. 2014a). In this sub-grid scale (SGS) model, the unknown SGS turbulent stresses produced by the filtering operation in Eq. (5) need a closure. Considering the Boussinesq approximation, the relationship between the anisotropic part of the SGS stress tensor and the large scale (i.e., resolved) strain rate tensor can be defined as

$$\tau_{ij}-\frac{1}{3}\delta_{ij}\tau_{kk}=-2\nu_{\mathrm{T}}\overline{S}_{ij},\quad \overline{S}_{ij}=\frac{1}{2}\left(\frac{\partial\overline{u}_i}{\partial x_j}+\frac{\partial\overline{u}_j}{\partial x_i}\right) \tag{8}$$

The isotropic part of stress tensor $\left(\frac{1}{3}\delta_{ij}\tau_{kk}\right)$ is implicitly added to the pressure. The SGS eddy-viscosity ν_{T} is a scalar quantity and is determined as

$$\nu_{\mathrm{T}}=C_\mu\overline{\Delta}^2\overline{S} \tag{9}$$

where C_μ is a model coefficient, $\overline{S}=\sqrt{2\overline{S}_{ij}\overline{S}_{ij}}$ is the invariant of resolved strain rate tensor and $\overline{\Delta}$ is the grid filter length

(or width) calculated from the cell volume:

$$\overline{\Delta} = (\Delta_1 \Delta_2 \Delta_3)^{\frac{1}{3}} \tag{10}$$

where Δ_1, Δ_2 and Δ_3 are the grid sizes in x, y and z directions, respectively. The eddy-viscosity coefficient C_μ appearing in Eq. (9) is a sensitive flow dependent quantity which can be computed as a scalar function of the invariants formed on the resolved strain rate $\overline{S}_{ij}$ tensor and the resolved vorticity tensor given by

$$\overline{W}_{ij} = \frac{1}{2}\left(\frac{\partial \overline{u}_i}{\partial x_j} - \frac{\partial \overline{u}_j}{\partial x_i}\right) \tag{11}$$

The invariants of resolved strain rate and vorticity tensors are defined by $S = \sqrt{2\overline{S}_{ij}\overline{S}_{ij}}$ and $W = \sqrt{2\overline{W}_{ij}\overline{W}_{ij}}$, respectively.

The SGS turbulent kinetic energy k_{sgs} transport model is responsible for the history and non-local effects, having the ability to model the complex flows with non-equilibrium characteristics. The SGS kinetic energy is defined as

$$k_{\text{sgs}} = \frac{1}{2}\tau_{kk} = \frac{1}{2}(\overline{u_k u_k} - \overline{u}_k \overline{u}_k) \tag{12}$$

The RAST model k_{sgs} is computed algebraically as

$$k_{\text{sgs}} = C_\mu^{\frac{2}{3}} (\overline{\Delta} \overline{S})^2 \tag{13}$$

The formulation for C_μ as suggested by Rahman and Siikonen (2006) in an RANS modeling is adapted with the RAST model:

$$C_\mu = \frac{1}{2(1 + T_{\text{t}} \overline{S}\sqrt{1 + \Re^2})} \tag{14}$$

where T_{t} is the hybrid time scale calculated as (Taghinia et al. 2015):

$$T_{\text{t}} = \sqrt{\frac{k^2}{\varepsilon^2} + C_{\text{T}}^2 \frac{\nu}{\varepsilon}} = \frac{k}{\varepsilon}\sqrt{1 + \frac{C_{\text{T}}^2}{Re_{\text{T}}}}, \quad Re_{\text{T}} = \frac{k^2}{\nu\varepsilon} \tag{15}$$

where Re_{T} is the turbulent Reynolds number and $C_{\text{T}} = \sqrt{2}$ is an empirical constant. $\Re = \left|\overline{W} / \overline{S}\right|$ is a dimensionless parameter which determines the flow characteristics (i.e., pure shear flow or plane strain flow). Therefore, C_μ given by Eq. (9) is appropriate for both the shear and vorticity dominated flows that are far from equilibrium. The strain dependent coefficient C_μ in the eddy-viscosity equation acts as a natural damping when approaching a wall. This feature provides a significant capability in the computation of flows with separation and reattachment.

The sub-grid heat fluxes are modeled using the gradient transport hypothesis (i.e., an eddy-viscosity formulation as well):

$$h_j = \alpha_{\text{sgs}} \frac{\partial \overline{\theta}}{\partial \overline{u}_j}, \quad \alpha_{\text{sgs}} = \frac{\nu_{\text{sgs}}}{Pr_{\text{sgs}}} \tag{16}$$

where Pr_{sgs} defines the turbulent sub-grid scale Prandtl number. Following the work by Murakami et al. (1995), the Pr_{sgs} value has been set to 0.5. This value implicitly implies that the characteristic length scale of the sub-grid scale turbulent fluctuations of the temperature is of the same order of the sub-grid scale turbulent flow motions.

2.2 SST–SAS model

The SAS is an alternative method to DES (detached eddy simulation) in which the RANS model is not influenced by the grid spacing. It is based on the SST k–ω turbulence model and modifies SST by adding a source term with the ω-equation to account for unsteadiness. The SST–SAS model solves transport equations for the turbulent kinetic energy k and the specific dissipation rate ω (Menter 1994; Menter and Egorov 2010):

$$\frac{\partial k}{\partial t} + \frac{\partial (\overline{u}_j k)}{\partial x_j} = \frac{\partial}{\partial x_j}\left[\left(\nu + \frac{\nu_{\text{T}}}{\sigma_{\text{k}}}\right)\frac{\partial k}{\partial x_j}\right] + P_{\text{k}} - \beta^* k\omega \tag{17}$$

$$\frac{\partial \omega}{\partial t} + \frac{\partial (\overline{u}_j \omega)}{\partial x_j} = \frac{\partial}{\partial x_j}\left[\left(\nu + \frac{\nu_{\text{T}}}{\sigma_\omega}\right)\frac{\partial \omega}{\partial x_j}\right] - \beta\omega^2 + P_\omega + 2(1 - F_1)\sigma_{\omega 2}\frac{1}{\omega}\frac{\partial k}{\partial x_i}\frac{\partial \omega}{\partial x_i} + P_{\text{SAS}} \tag{18}$$

where ν is the kinematic viscosity, the production term $P_{\text{k}} = -\tau_{ij}$.

The bar $(\overline{\cdot})$ over the velocity components in Eqs. (17) and (18) denotes time averaging for the RANS and filtering (volume averaging) for the LES. The eddy-viscosity ν_{T} is computed as

$$\nu_{\text{T}} = \frac{a_1 k}{\max(a_1 \omega, SF_2)} \tag{19}$$

where $a_1 = 0.31$ and $\overline{S} = \sqrt{2\overline{S}_{ij}\overline{S}_{ij}}$ is the absolute value of the mean strain rate tensor. Other model parameters are

$$P_\omega = \gamma \frac{P_{\text{k}}}{\nu_{\text{T}}}, \quad F_1 = \tanh(\xi^4)$$

$$\xi = \min\left[\max\left\{\frac{\sqrt{k}}{\beta^* \omega y}, \frac{500\nu}{\omega y^2}\right\}, \frac{4\sigma_{\omega 2} k}{\text{CD}_\omega y^2}\right]$$

$$\mathrm{CD}_{\omega} = \max\left(\frac{2\sigma_{\omega 2}}{\omega}\frac{\partial k}{\partial x_i}\frac{\partial \omega}{\partial x_i}, 10^{-10}\right)$$

$$F_2 = \tanh\left[\left\{\max\left(\frac{2\sqrt{k}}{\beta^*\omega y}, \frac{500\nu}{\omega y^2}\right)\right\}^2\right]$$

The model coefficients in Eqs. (17) and (18) are obtained from

$$\left(\sigma_{\mathrm{k}}\ \sigma_{\omega}\ \beta\right)^{\mathrm{T}} = F_1\left(\sigma_{\mathrm{k}}\ \sigma_{\omega}\ \beta\right)_1^{\mathrm{T}} + (1-F_1)\left(\sigma_{\mathrm{k}}\ \sigma_{\omega}\ \beta\right)_2^{\mathrm{T}}$$

with the following values

$$\sigma_{\mathrm{k}1} = 1.176, \quad \sigma_{\omega 1} = 2.0, \quad \beta_1 = 0.075$$
$$\sigma_{\mathrm{k}2} = 1.0, \quad \sigma_{\omega 2} = 1.168, \quad \beta_2 = 0.0827$$

The coefficient γ is calculated from

$$\gamma = \frac{\beta}{\beta^*} - \frac{\kappa^2}{\sigma_{\omega}\sqrt{\beta^*}}$$

with $\kappa = 0.41$ and $\beta^* = 0.09$.

The quantity P_{SAS} in Eq. (18) is an additional production term, extracted from a combination of k–kl (Rotta 1951) and k–ω turbulence models. The source term P_{SAS} can be expressed as follows (Winkler et al. 2011):

$$P_{\mathrm{SAS}} = \max\left[\zeta\kappa\overline{S}^2\left(\frac{L}{L_{\mathrm{vK}}}\right)^2 - 6k\max\left\{\frac{1}{\omega^2}\left(\frac{\partial\omega}{\partial x_i}\right)^2, \frac{1}{k^2}\left(\frac{\partial k}{\partial x_i}\right)^2\right\}, 0\right] \tag{20}$$

where $\zeta = 3.51$, $L = \sqrt{k}/\left(C_{\mu}^{1/4}\omega\right)$ and $C_{\mu} = \beta^*$.

The SAS model provides for the direct control of the high wave number damping using the approach to introducing the explicit limitation of L_{vK} by the grid spacing $\overline{\Delta}$ with the SST–SAS model:

$$L_{\mathrm{vK}} = \max\left(\kappa\frac{\overline{S}}{U''}, \overline{C}_{\mathrm{s}}\overline{\Delta}\right) \tag{21}$$

where $U'' = \left|\nabla^2\overline{u}\right|$ and $\overline{\Delta}$ is the cubic root of the cell volume V (i.e. $\overline{\Delta} = V^{\frac{1}{3}}$) and $\overline{C}_{\mathrm{s}}$ is the Smagorinsky coefficient ($\overline{C}_{\mathrm{s}}$ could be a constant/variable depending on an LES model used). To eliminate any possible criticism of the SAS behavior in the infinite grid limit, it is preferred to limit the predicted eddy-viscosity by the eddy-viscosity of an LES model (Taghinia et al. 2014b):

$$\nu_{\mathrm{T}} = \max\left(\nu_{\mathrm{T}}^{\mathrm{SAS}}, \nu_{\mathrm{T}}^{\mathrm{LES}}\right) \tag{22}$$

In the present study, a dynamic Smagorinsky model (DSM) is used that would produce an essentially zero $\nu_{\mathrm{T}}^{\mathrm{LES}}$ in RANS regions, especially close to the walls.

3 Computational aspects

The filtered incompressible Navier–Stokes equations are solved using a finite volume method formulated on a collocated grid arrangement. The continuity and momentum equations are coupled using the PISO (Pressure Implicit Splitting of Operators) algorithm with two corrector steps which ensure mass conservation. A Rhie–Chow interpolation is used for the pressure gradient terms to avoid pressure oscillations due to the collocated grid arrangement (Rahman et al. 1996, 1997). A second-order upwind flux difference splitting scheme for convective terms and a central differencing scheme for diffusion terms are applied. For time integration, a Crank–Nicolson second-order accurate scheme is utilized. An algebraic multi-grid method is employed to accelerate the solution convergence. The present numerical method and the applied solver have been tested extensively by computing several laminar and turbulent flows (Majander 2000; Davidson 2001; Krajnovic and Davidson 2006; Majander and Siikonen 2002).

In order to analyse the performance of a recently developed zero-equation model RAST for indoor airflows, three ventilation cases with a forced convection, a mixed convection and an isothermal impinging jet in a room are investigated. For a better evaluation of the accuracy of RAST model, computations are compared with those obtained using the SST–SAS hybrid model. As the sub-grid scale model is highly dependent on the grid resolution, the grid size is set in a way that the thickness of the first near wall cell is below 1 in y^+ unit, required by an LES to produce a correct near wall behavior.

A no-slip boundary condition is imposed on solid walls. A non-reflective convective boundary condition $\partial\overline{u}_i/\partial t + U_{\mathrm{c}}\partial\overline{u}_i/\partial x = 0$ is applied at the outflow, ensuring that the flow leaves the computational domain. The convection speed U_{c} is set equal to the exit mean velocity. The inlet boundary condition is constructed from a separate LES computation for a periodic channel/pipe flow with a length of $10h_{\mathrm{in}}$ (h_{in} is the inlet slot height or diameter). The Reynolds number is identical to that of the channel/pipe upstream of the flow. For SST–SAS calculations, k and ω at the inlet are calculated as $k_{\mathrm{in}} = \frac{1}{2}(U_{\mathrm{in}}T_{\mathrm{i}})^2$ and $\omega_{\mathrm{in}} = k_{\mathrm{in}}^{\frac{1}{2}}/C_{\mu}^{\frac{1}{4}}l$ where T_{i} is turbulent intensity, ω_{in} is the specific dissipation rate, $C_{\mu} = 0.09$, and l is the turbulent length scale.

The dimensionless time step $\Delta t U_{\mathrm{in}}/h_{\mathrm{in}}$ is chosen in a way that corresponds to the maximum Courant–Friedrichs–Lewy (CFL) number of 0.6; this guarantees the required stability criteria in numerical schemes. The statistics are obtained when the flow reached the statistically steady-state

and the averaging is performed over 800–1000 dimensionless time steps. To accelerate the calculation time, a k–ε model (Rahman and Siikonen 2006) is used to calculate each case with the respective grid. The LES calculations are initiated from a fully converged k–ε results.

4 Results and discussion

4.1 Forced convection

The computational domain follows the experimental work of Nielsen et al. (1978) as shown in Fig. 1. In their experiments the measurements are performed on a scale model of the indoor airflow with $W/H=1$ and $L/H=3$. The inlet slot height $h_{in}/H=0.056$ and outlet slot height $h_{out}/H=0.16$. The slot width of the inlet and outlet is the same as the model width. The Reynolds number is $Re=U_{in}h_{in}/\nu=5\times10^3$ based on the inlet slot height. A grid distribution of $140\times120\times120$ is used in the x (length), y (height) and z (width) directions, respectively (Fig. 2). According to the grid dependent study (not shown), this grid size has produced relatively accurate results compared with the experiment and applying finer grids does not produce any noticeable differences or improvements (about 2%). A higher resolution grid distribution is considered with a grid stretching ratio of 1.06 at near wall regions in order to capture all flow information. This grid distribution satisfies $y^+<1$ condition which is essential to resolve all turbulent structure close to the wall. A dimensionless time step $\Delta tU_{in}/h_{in}=0.001$ is used in this simulation. The time averaging is initiated when a statistical convergence is achieved. The averaging procedure is performed for 1000 dimensionless time steps.

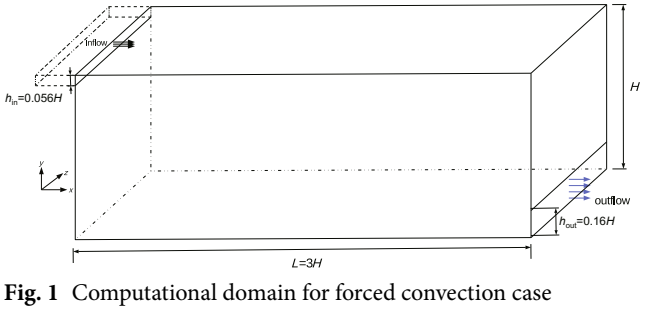

Fig. 1 Computational domain for forced convection case

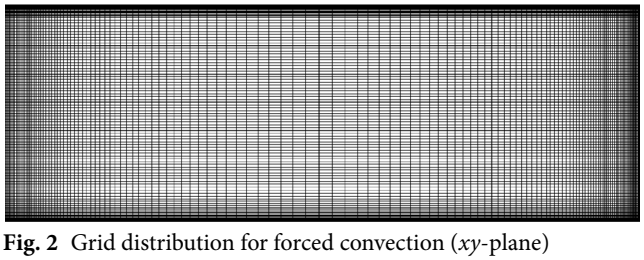

Fig. 2 Grid distribution for forced convection (xy-plane)

The mean velocity and fluctuation profiles at horizontal y/H (=0.028, 0.972) and vertical x/H (=1, 2) locations are demonstrated in Figs. 3 and 4, respectively. As shown in Fig. 3, both model predictions agree well with the experimental data; however, the RAST model shows a better agreement with measurements (3% difference) as the flow travels away from the inlet. Considering the mean velocity distribution at x/H = 1 and x/H = 2, RAST model predictions agree with the experimental data very well close to the wall region (with less than 3% error) due to its sensitivity to the recirculation and streamline curvature.

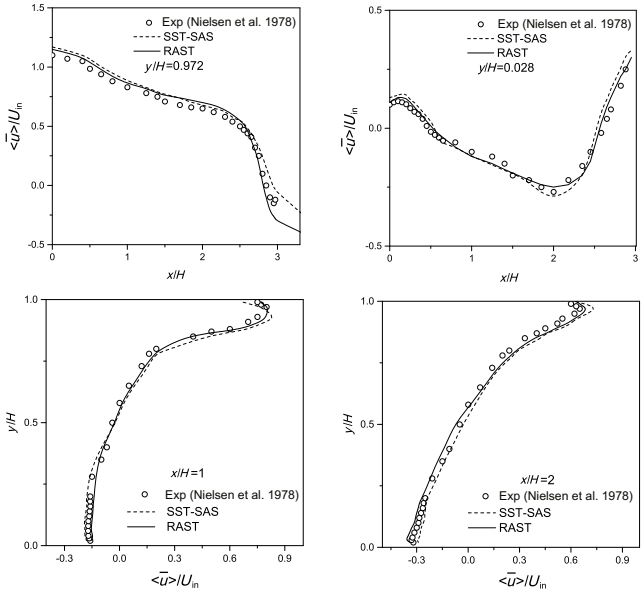

Fig. 3 Predicted mean velocity profiles at different locations for forced convection

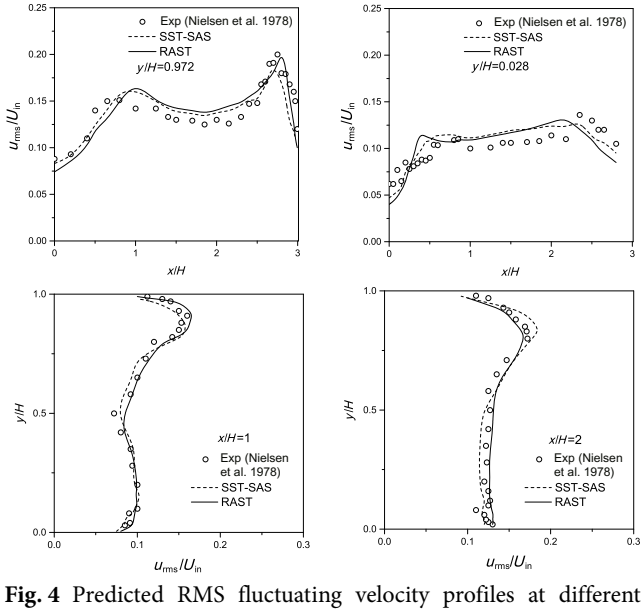

Fig. 4 Predicted RMS fluctuating velocity profiles at different locations for forced convection

On the other hand, the turbulent eddy-viscosity of SST–SAS model is under-predicted close to the top wall (the jet region) causing an over-prediction of the mean velocity in that location. Overall, the trend and magnitude of the predicted velocities are almost the same for both models; however RAST shows a better performance close to the top and bottom walls.

Figure 4 shows the root-mean-square (RMS) velocity fluctuations values for RAST and SST–SAS models. A lower turbulent fluctuations at $y/H = 0.972$ and $y/H = 0.028$ is due to the under-estimation of turbulent eddy-viscosity in SST–SAS model which can explain the discrepancies between the computed results and measured data of mean velocity close to the wall at these locations. Both model predictions are consistent with the experimental data at $x/H = 1$ and $x/H = 2$ with a maximum deviation of 5%; however RAST model gives more accurate results in terms of turbulence statistics.

4.2 Mixed convection

This section presents the results for a mixed convection which is a common phenomenon in a room ventilation system. The simulation replicates the experimental work of Baly et al. (1992). They measured the air velocity, temperature and turbulence kinetic energy. Figure 5 illustrates the geometry for the mixed convection with the dimensions of $H = 1.04$ m high, $L = 1.04$ m long and $W = 0.7$ m wide. Following the experiment of Baly et al. (1992), the inlet and the outlet slot height are $h_{in} = 0.018$ m and $h_{out} = 0.024$ m respectively. The inlet velocity $U_{in} = 0.57$ m/s and temperature $T_{in} = 15$℃ according to the experiment with $Re = 678$. The floor temperature is maintained at $T_f = 35$℃; all other walls have the same temperature of $T_w = 15$℃. The meshes employed are $160 \times 160 \times 120$ for the x, y and z directions, respectively. The mesh is stretched with a growth ratio of 1.08 in wall normal directions. A dimensionless time step of $\Delta t U_{in} / h_{in} = 0.001$ is used, corresponding to a maximum Courant (CFL) number of around 0.5. Calculations are performed for 1000 dimensionless time steps to make sure that the flow is statistically converged.

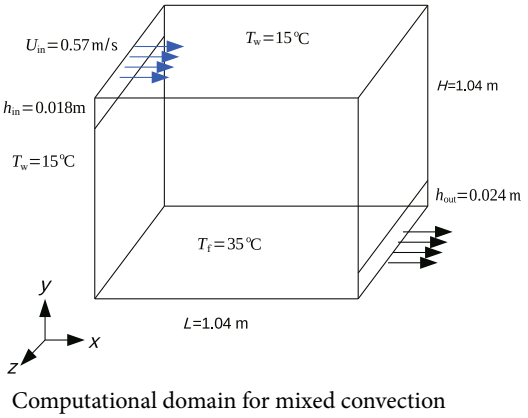

Fig. 5 Computational domain for mixed convection

The predicted results for mean air velocity at two center plane $x/L = 0.5$ and $y/L = 0.5$ are shown in Fig. 6. The predicted velocity profiles for both models agree well with the experimental data having less than 3% error. However, the RAST model performs slightly better than that of the SST–SAS. Figure 7 illustrates the computed total turbulence kinetic energy at the same sections mentioned above and the comparison with the corresponding experimental data. Evidently, the predicted turbulence kinetic energy profile is the same as the experimental one. Figure 8 compares the predicted mean temperature profiles with the measured data at the two mid-planes. In terms of temperature distribution, both the models reproduce almost identical values which are in a good agreement with measured ones (with a maximum of 3% deviation).

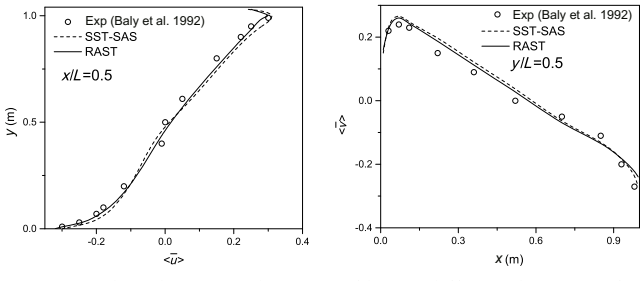

Fig. 6 Predicted mean velocity profiles at different locations for mixed convection

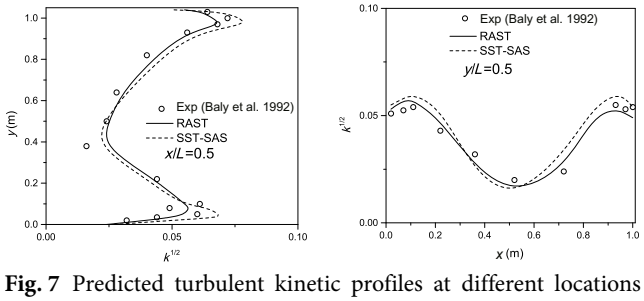

Fig. 7 Predicted turbulent kinetic profiles at different locations for mixed convection

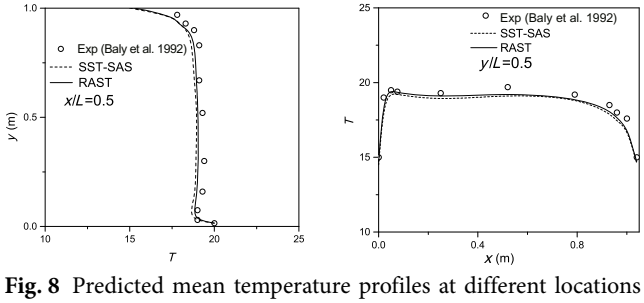

Fig. 8 Predicted mean temperature profiles at different locations for mixed convection

4.3 Isothermal impinging jet

The impinging jet ventilation process provides better air distribution through the conventional mixing and displacement ventilation as well as capability for both cooling and heating purposes. The structure of flow in impinging jet enables the air to overcome the buoyancy force and reaches further distances; therefore it provides a more efficient way to ventilate air in various indoor environments. This section represents the results for an impinging jet in a room. The simulation setting follows the experimental study of Chen et al. (2012). The measurement is carried out for a semi-confined room with the size of $5.76\,\text{m} \times 3.04\,\text{m} \times 3\,\text{m}$. There are three openings (outlets) inside the room; two of them are 1 m high and 5.76 m long, located below two side walls (Fig. 9). The third opening is situated at the end of the room with 3 m height and 1.32 m width. A semi-elliptic duct located at $h = 0.6$ m above the floor, injects air into the room. The geometry and dimension of the supply duct at the outlet are also shown in Fig. 9.

The incoming air velocity is $V_{in} = 1.2$ m/s. The inlet condition is obtained from a separate LES of a fully developed turbulent pipe flow with the same diameter in order to produce a more realistic boundary condition at the exit of the nozzle. An atmospheric pressure boundary condition is applied for the two openings below the side walls. At the other end of the room where the door (outlet) is situated, a convective boundary condition is implemented to drive the flow out of the domain (as described in Section 3).

A grid independency tests is performed using three different grid distributions with 4×10^6, 6.5×10^6 and 8×10^6 cells, respectively. Numerical results (not reproduced herein) showed that predictions of last two grids were almost identical (about 2% difference) to each other; therefore, the grid distribution with 6.5×10^6 cells is considered for validations. Figure 10 shows the grid distribution for the simulated room. The grids near the wall are constructed in a way to ensure $y^+ < 1$. A time step of $\Delta t U_{in} / d = 0.001$ is used in the calculations. As a statistically steady-state is achieved for the simulation, the time averaging is performed over 800 dimensionless time steps.

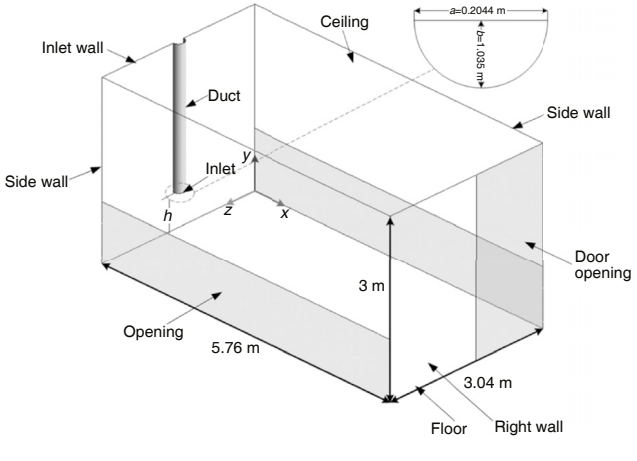

Fig. 9 Computational domain for impinging jet in a room

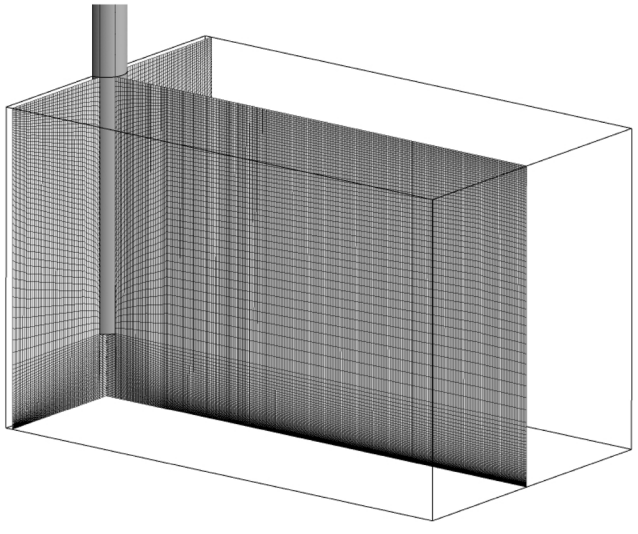

Fig. 10 Mesh distribution for impinging jet in a room

Figures 11 and 12 demonstrates the jet velocity distributions computed from the RAST model and SST–SAS with experimental data (Chen et al. 2012). Results are extracted at various locations in the vertical middle plane, regions below the inlet and along the floor. The velocity is normalized by a local maximum velocity U_{max} or V_{max} and the distance x or y is scaled with a hydraulic diameter $d = 0.1265$ m. The comparisons are performed at four downstream distances from the inlet wall and presented in terms of the mean velocity distribution in Fig. 11. As the flow travels away from the inlet, the predicted velocity profiles from both

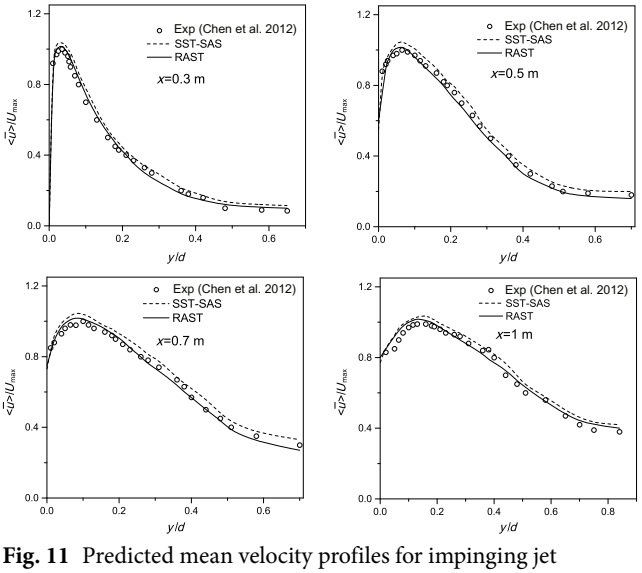

Fig. 11 Predicted mean velocity profiles for impinging jet

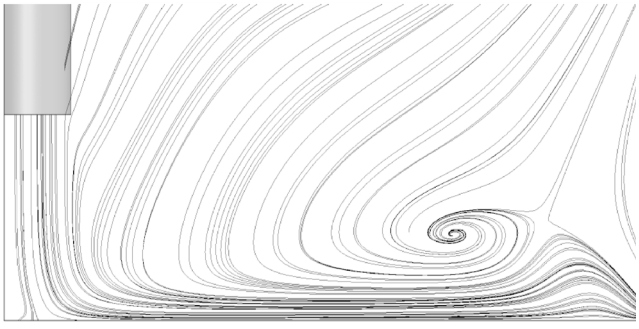

Fig. 12 Averaged streamlines predicted by RAST model below the inlet

models show a good agreement with the experimental data. The averaged streamlines predicted by the RAST model are illustrated in Fig. 12. As can be seen after jet impacts with the floor, it looses kinetic energy and smoothly travels along the floor toward the other end of the room. The velocity difference between various regions in the room, creates a recirculation region. In general, the RAST model produces slightly better results in the whole flow region of the room. Jet profiles below the inlet are shown in Fig. 13; the predicted jet profiles from both turbulence models show a good consistency with the experimental data beneath the inlet having less than 3% deviation from measurements. The predictions from the two models are quite similar in various zones. However, it is should be mentioned that the flow velocity is well captured by the RAST model compared to the SST–SAS, especially at $0 < x/d < 0.6$.

The maximum velocity decay in the regions below the exit and along the centerline of the floor is displayed in Fig. 14. As the jet reaches the floor, the predicted decaying velocity from both models show same behavior as the experimental values. From these profiles, it can be understood

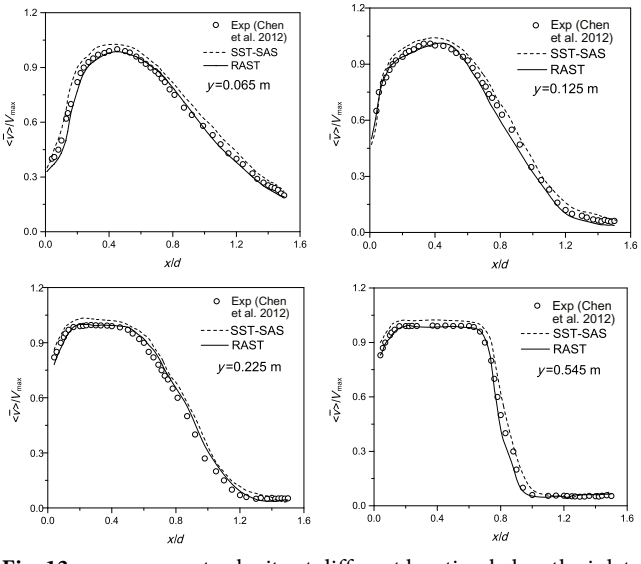

Fig. 13 y-component velocity at different location below the inlet

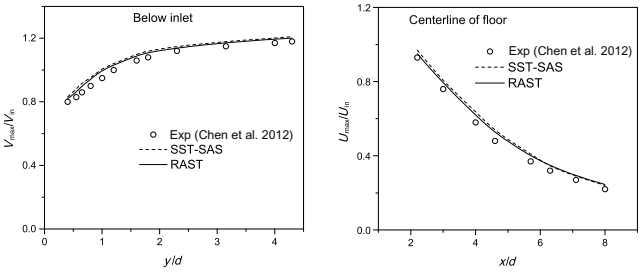

Fig. 14 Jet maximum velocity decay at different locations

that in the most of sampled regions the velocity decays slowly. This is mainly due to the effect of turbulence shear stress on the jet behavior. After the jet impinges on the floor, the flow is reflected and proceeds along the floor. At a further downstream of the impingement area, the flow expands along the floor and transforms to a thin shear layer. As can be seen, both models are in close agreement with experiments showing between 2% and 3% error. It seems likely that both the models are able to capture the mean flow field of an isothermal impinging jet in a room satisfactorily.

5 Conclusions

The current study is focused on the application and performance of two turbulence approaches in an indoor airflow simulation: the RAST model with a single grid filter and the SST–SAS hybrid RANS–LES. RAST model does not need any ad hoc clipping of averaging for the eddy-viscosity coefficient for numerical stabilization; instead it is dependent on the rotational and irrotational strains producing natural damping as the wall is approached. The performance and assessment of both models are examined for the forced and mixed convection as well as the impinging jet in a room. The predicted results dictate that both the models can provide an accurate and reliable information on the main features of flow in enclosed spaces such as velocity and temperature distributions close to the walls as well as predicting the correct level of kinetic energy. However, the RAST capabilities in reproducing the flow structures and statistics are slightly better than that of the SST–SAS model, especially in predicting the velocity distribution for the forced convection and impinging jet cases. It is worthwhile mentioning that the computational effort for the RAST model is almost the same as that of the SST–SAS model.

References

Baly D, Mergui S, Niculae C (1992). Confined turbulent mixed convection in the presence of a horizontal buoyant wall jet. In: Chen TS, Chu TY, eds, Fundamentals of Mixed Convection, HTD–Vol 213, New York: ASME, pp. 65–72.

Cao GY, Ruponen M, Paavilainen R, Kurnitski J (2011). Modeling and simulation of the near-wall velocity of a turbulent ceiling attached plane jet after its impingement with the corner. *Building and Environment*, 46: 489–500.

Chen HJ, Moshfegh B, Cehlin M (2012). Numerical investigation of the flow behavior of an isothermal impinging jet in a room. *Building and Environment*, 49: 154–166.

Chen Q (1995). Comparison of different k–ε models for indoor air flow computations. *Numerical Heat Transfer, Part B*: *Fundamentals*, 28: 353–369.

Chen Q (1996). Prediction of room air motion by Reynolds-stress model. *Building and Environment*, 31: 233–244.

Chen Q (1997). Computational fluid dynamics for HVAC: Successes and failures. *ASHRAE Transactions*, 103(1): 178–187.

Cheng Y, Lien FS, Yee E, Sinclair R (2003). A comparison of large eddy simulations with a standard k–ε Reynolds-averaged Navier–Stokes model for the prediction of a fully developed turbulent flow over a matrix of cubes. *Journal of Wind Engineering and Industrial Aerodynamics*, 91: 1301–1328.

Davidson L (2001). Hybrid LES–RANS: A combination of a one-equation SGS model and a k–ω model for predicting recirculating flows. In: Proceedings of ECCOMAS CFD Conference, Swansen, UK.

Germano M, Piomelli U, Moin P, Cabot WH (1991). A dynamic subgrid-scale eddy viscosity model. *Physics of Fluids A*: *Fluid Dynamics*, 3: 1760–1765.

Heschl C, Inthavong K, Sanz W, Tu J (2013). Evaluation and improvements of RANS turbulence models for linear diffuser flows. *Computers & Fluids*, 71: 272–282.

Krajnovic S, Davidson L (2006). A mixed one-equation subgrid model for large-eddy simulation. *International Journal of Heat and Fluid Flow*, 27: 402–415.

Luo S, Roux B (2004). Modeling of the HESCO nozzle diffuser used in IEA annex 20 experimental test room. *Building and Environment*, 39: 367–384.

Majander P (2000). Developments in large eddy simulation. Report 128, Aalto University.

Majander P, Siikonen T (2002). Large-eddy simulation of a round jet in a cross-flow. *International Journal of Heat and Fluid Flow*, 23: 413–425.

Menter FR (1994). Two-equation eddy-viscosity turbulence model for engineering application. *AIAA Journal*, 32:1598–1605.

Menter FR, Egorov Y (2010). The scale-adaptive simulation method for unsteady turbulent flow predictions. Part 1: Theory and model description. *Flow, Turbulence and Combustion*, 85: 113–138.

Murakami S, Mochida A, Matsui K (1995). Large eddy simulation of non-isothermal room airflow, comparison between standard and dynamic type of Smagorinsky model, SEISAN-KENKYU. *Journal of Institute of Industrial Science*, 4(2): 7–12.

Nielsen PV, Restivo A, Whitelaw JH (1978). The velocity characteristics of ventilated room. *ASME Journal of Fluids Engineering*, 100: 291–298.

Rahman MM, Miettinen A, Siikonen T (1996). Modified SIMPLE formulation on a collocated grid with an assessment of the simplified QUICK scheme. *Numerical Heat Transfer, Part B*: *Fundamentals*, 30: 291–314.

Rahman MM, Siikonen T, Miettinen A (1997). A pressure-correction method for solving fluid flow problems on a collocated grid. *Numerical Heat Transfer, Part B*: *Fundamentals*, 32: 63–84.

Rahman MM, Siikonen T (2006). An explicit algebraic Reynolds stress model in turbulence. *International Journal of Numerical Methods in Fluids*, 52: 1135–1157.

Rotta JC (1951). Statistische Theorie Nichthomogener Turbulenz. *Zeitschrift fur Physik*, 129: 547–572. (in German)

Smagorinsky J (1963). General circulation experiments with the primitive equations, I. The basic experiment. *Monthly Weather Review*, 91: 99–164.

Stamou A, Katsiris I (2006). Verification of a CFD model for indoor airflow and heat transfer. *Building and Environment*, 41: 1171–1181.

Taghinia J, Rahman MM, Siikonen T, Agarwal RK (2014a). A sub-grid scale model with non-traditional eddy-viscosity coefficient. In: Proceedings of 7th AIAA Theoretical Fluid Mechanics Conference.

Taghinia J, Rahman MM, Siikonen T (2014b). Numerical investigation of twin-jet impingement with hybrid-type turbulence modeling. *Applied Thermal Engineering*, 73: 648–657.

Taghinia J, Rahman MM, Siikonen T, Agarwal RK (2015). One-equation subgrid scale model with variable eddy-viscosity coefficient. *Computers & Fluids*, 107: 155–164.

Winkler CM, Dorgan AJ, Mani M (2011). Scale adaptive simulations of turbulent flows on unstructured grids. In: Proceedings of 20th AIAA Computational Fluid Dynamics Conference, Honolulu, USA.

Zhai Z, Zhang Z, Zhang W, Chen Q (2007). Evaluation of various turbulence models in predicting airflow and turbulence in enclosed environments by CFD. Part 1: Summary of prevalent turbulence models. *HVAC&R Research*, 13: 853–870.

Zhang Z, Zhang W, Zhai JZ, Chen Q (2007). Evaluation of various turbulence models in predicting airflow and turbulence in enclosed environments by CFD. Part 2: Comparison with experimental data from literature. *HVAC&R Research*, 13: 871–886.